# Elucidating the role of soil hydraulic properties on aspect-dependent landslide initiation

Yanglin Guo[1, 2], Chao Ma[1, 2]

1. School of Soil and Water Conservation, Beijing Forestry University, Beijing 100083, PR China.

2. Jixian National Forest Ecosystem Observation and Research Station, CNERN, Beijing Forestry University, Beijing 100083, PR China.

Corresponding Author: Professor Chao Ma, sanguoxumei@163.com

**Abstract:** Aspect-dependent landslide initiation is an interesting finding, and previous studies have attributed this to the mechanical effects of plant roots. In the present study, an overwhelming landslide probability on a south-facing slope over a north-facing slope was found in a localized area with only granite underneath and high cover of *Larix kaempferi*. These observations cannot be attributed to plant roots but may result from factors related to hillslope hydrology. Differential weathering associated with hillslope hydrology behaviors such as rainfall water storage and leakage, pore water pressure, particle component, and hillslope stability fluctuation were used to examine these observations. Remote sensing interpretation using the high-resolution GeoEye-1 image and digitalized topography showed that landslides on south-facing slopes have a higher probability, larger basal area, and shallower depth than those on a north-facing slope. The lower limits of the upslope contributing area and slope gradient condition for south-facing landslides were less than those for north-facing landslides. The higher basal areas of south-facing landslides than those of the north-facing landslides may be attributed to the high peak values and slow dissipation of pore water pressure. The absorbed and drained water flow in a given time interval, together with the calculated water storage and leakage during the measured rainy season measured, demonstrate that the soil mass above the failure zone for south-facing slopes is more prone to pore-water pressure, which results in slope failures. In comparison, the two stability fluctuation results from the finite and infinite models further verified that landslides on south-facing slopes may fail under conditions of prolonged antecedent precipitation and intensive rainfall. Meanwhile, those on north-facing slopes may fail only in response to intensive rainfall. The results of this study will deepen our knowledge of aspect-dependent landslide initiation from both classical mechanics and the state of stress.

**Keywords: Landslide; Pore pressure; suction stress; Hydraulic conductivity; Slope stability**

## 1 Introduction

In some semi-arid environments of the Northern Hemisphere, aspect-dependent landslide initiation provides valuable insights into the relative importance of different factors in developing accurate landslide susceptibility models (Ebel, 2015; Rengers et al., 2016; Li et al., 2021; Deng et al., 2022). These events provide a thorough understanding of the amount of direct sunlight that translates into differences in vegetation communities, bedrock weathering, and soil development processes (Fu, 1983; Wang, 2008; Bierman and Montgomery, 2014). These earth surface processes indirectly affect hillslope hydrology and landscape dissection at the hillslope scale. Rainfall-induced shallow landslides are geomorphic agents at the hillslope scale and are governed by multiple factors, including hydrology, hillslope materials, bedrock, and vegetation (Birkeland, 1999; Geroy et al., 2011; Lu and Godt, 2013). Currently, the aspect-dependent landslide initiation observed has been predominantly attributed to the mechanical effect of plant roots. This is because the differences in vegetation on the south- and north-facing slopes are easier to examine and more pronounced than other factors (Li et al., 2021; Timilsina et al., 2021; Dai et al., 2022; Deng et al., 2022). However, vegetation succession takes place over substantially longer timescales than soil development and bedrock weathering (Watakabe and Matsushi, 2019). In most cases, the plant roots are not deep enough to penetrate into the bedrock (Schwinning, 2010). Hypothesizing for a relatively localized area with the same ecosystem or plant species, aspect-dependent landslide initiation cannot be attributed to plant roots but may result from differences in the properties of hillslope materials due to long-term differential weathering.

43    Aspect-dependent landslides in Frontal Colorado, USA and the Loess Plateau, China, have attracted interest
44    because vegetation has a considerable influence on landslide distribution. The strong propensity for shallow landslide
45    initiation on south-facing hillslopes in the two regions is closely related to the present-day tree density, regardless of
46    the hillslope aspect (Ebel, 2015; Rengers et al., 2016; Deng et al., 2022). In the Colorado Frontal Range, field
47    observations have shown that south-facing slopes lack thick tree cover and have an abundance of rock outcrops
48    compared to north-facing slopes. In addition, the soil layer is thinner on south-facing slopes (Coe et al., 2014; Ebel
49    et al., 2015). The cohesion supplied by the roots is responsible for the connection observed between landslide
50    distribution and slope aspect (McGuire et al., 2016). On the Loess Plateau, vegetation recovery is one of the main
51    ecological measures for mitigating sediment loss (Fu et al., 2009). Increased soil strength and hydraulic conductivity
52    due to strong root networks may enhance the topographic initiation conditions (Montgomery and Dietrich, 1994;
53    Wang et al., 2020). North- and westward moving storms may potentially produce more intense rainfall on the south-
54    and east-facing slopes. This assumption may be invalid if an aspect-dependent landslide distribution is present in a
55    localized catchment with a specific vegetation community. This study highlights the effect of the mechanical function
56    of plants on landslides. If an aspect-dependent landslide exists in a localized area with vegetation cover comprising
57    the same plant species alongside a high level of vegetation cover, the aspect-dependent landslide initiation observed
58    cannot be attributed to the mechanical effect of plant roots.

59    To determine the relationship observed among vegetation, landslides, and slope aspect, the effects of the
60    physical properties and strength of hillslope materials cannot be excluded. On the northern part of the Loess Plateau,
61    China, as well as in many other semi-arid environments (Fu, 1983; Heimsath et al., 1997; Wang, 2008), different
62    types and densities of vegetation and soils develop on north-facing versus south-facing convergent slopes. This is
63    because systematic differences in the amount of direct sunlight translate into differences in physical and chemical
64    weathering. North-facing convergent slopes have lower evaporation rates, retain snow cover longer in spring, and
65    tend to hold soil moisture longer during the summer growing season. These differences may result in localized
66    ecosystem communities in the presence of trees or shrubs on grass. South-facing slopes experience heavier and more
67    frequent hydration, thermal expansion, or freeze-thaw cycles due to day warming and night cooling and tend to have
68    stronger weathering throughout the year. These differences can result in local differences in the grain component,
69    soil strength, and soil profile. This has indirect effects at the landslide scale through the mechanics of excessive pore
70    water pressure dissipation and sliding surface liquefaction (Terzaghi, 1950; Sassa, 1984), and hillslope hydrology
71    behavior (Godt et al., 2009; Lee and Kim, 2019). Therefore, the physical properties of hillslope materials may be
72    attributed to the aspect-dependent landslide initiation observed.

73    All shallow landslides are examples of debris flow initiation, which often enlarges their scale by multiple
74    mechanics (Hungr et al. 2005; Iverson et al. 2011). When the slope fails, the pore water pressure abruptly increases
75    within the shear zone (Iverson and LaHusen, 1989; Wang and Sassa, 2003). If the excessive pore water pressure
76    persists high over the static pressure for a relatively long duration, the displaced masses enlarge their volume by
77    widespread liquefaction and transform into debris flows (Bogaard and Greco, 2016). The magnitude of the pore
78    water pressure is closely related to the scale of the shallow landslide. Therefore, the scale of shallow landslides can
79    be determined by the role of excessive pore water pressure during the failure process. However, the aspect-dependent
80    landslide distribution in these two areas refers to the differences in landslide probability rather than the landslide
81    scale.

82    In the present study, we used a combination of field soil moisture observation, strength measurement, hydraulic
83    conductivity analysis of hillslope materials, and numerical modeling of slope stability to explain the high potential
84    for landslide initiation on south-facing slopes relative to north-facing slopes with the same vegetation communities.
85    Differences in landslide geometry and initiation conditions, in the form of the contributing area above the scar area
86    and the landslide gradient, were shown using field studies and high-resolution GeoEye-1 images. The differential

87  weathering-related physical properties and strength of the soil mass, including the dry unit weights, porosity, grain

88  size, effective cohesion, and inner friction angle were examined. We have also highlighted the importance of

89  excessive pore water pressure, hillslope hydrology, and stability in explaining the aspect-dependent landslide

90  initiation observed. The results of this work will deepen our understanding of aspect-dependent landslide distribution

91  in some mountainous areas of the Northern Hemisphere.
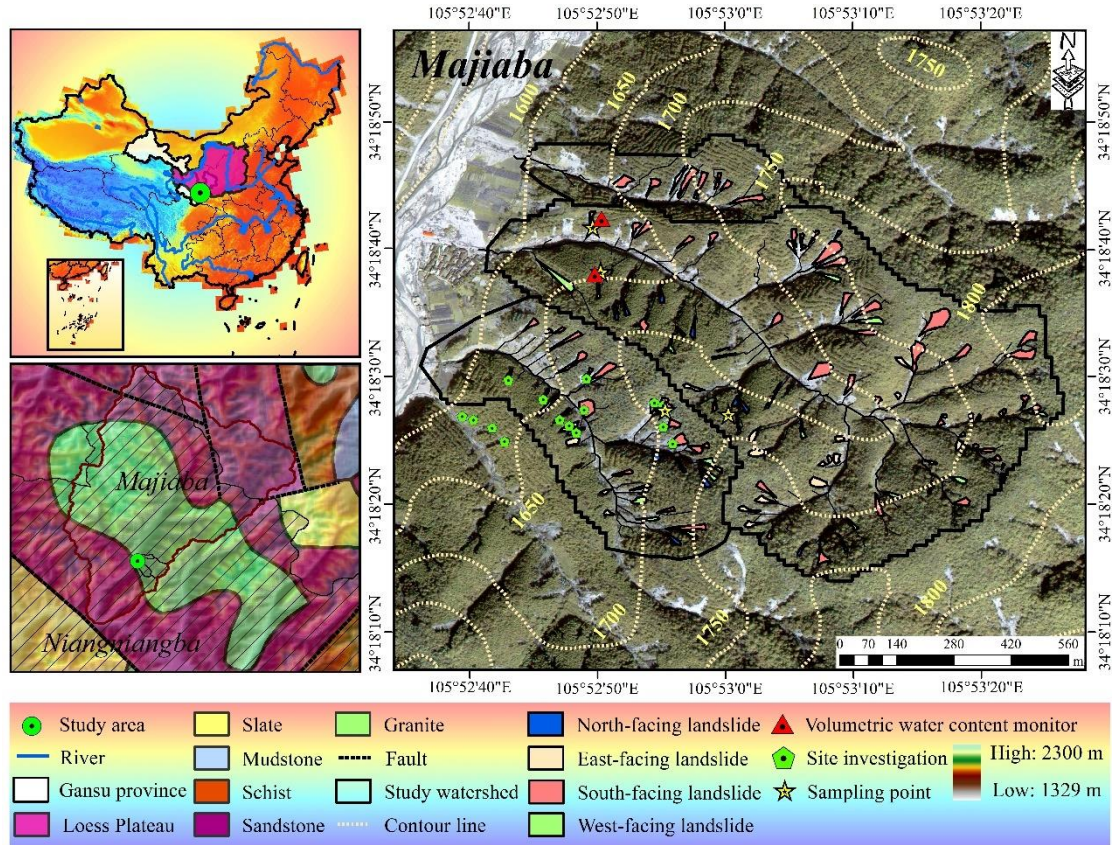
92

93  **Fig. 1.** Location, topography, and simplified lithology of the study area. All maps are created by the authors. The

94  graph of Majiaba was taken using an Unmanned Aerial Vehicle. The territorial domain of China and

95  simplified lithology map are from China Geological survey.

96  **2 Study area**

97  The study area is in the mountainous region of Majiaba village, northeast of Niangniangba town, Tianshui City,

98  Gansu Province, Central China. It is also close to the dividing crest of the Yellow and Yangtze Rivers and on the

99  eastern part of the Loess Plateau. Most of the hillslope is underlain by slate, and the stratigraphic units of granite,

100  sandstone, and mudstone account for a smaller area. This area has four distinctive seasons and a semi-humid climate.

101  The annual precipitation is approximately 491.6 mm and predominantly falls during June and August. One branch

102  fault of the Tianshui-Lanzhou fault system runs through the area and has had no rupture records for the last few

103  decades.

104  The shallow landslides in the study area and nearby surroundings were triggered by the prolonged antecedent

105  precipitation during July 1–24 and the intensive rainstorm on July 25, 2013 (Yu et al., 2014; Guo et al., 2015). Most

106  shallow landslides in the entire storm spanned the mountain area with a gradient of 20–25 °, located on south-facing

107  slopes and in areas with relatively sparse vegetation (Li et al., 2021). The strong root network may promote hydraulic

108  conductivity of the soil–root composite and the landslide initiation condition of the upslope contributing area–slope

109  gradient, according to the landslide case studies from the *Larix kaempferi* and *Pinus tabuleaformis* forests (Dai et

al., 2022). The three small catchment areas in the Majiaba Watershed are underlain by granite units. The total area is 0.88 km$^2$ with vegetation cover of over 90% (Fig. 1). The relative relief was approximately 200 m, and the mean hillslope gradient was 37°. The reason why the three catchments in the area were chosen is that the main plant species on the south- and north-facing slope is *Larix kaempferi*, which commonly have highly developed lateral roots with depth < 0.4 m. However, landslides in the three catchments still have a higher propensity for occurrence on south-facing slopes in comparison with the north-facing slopes. This finding differs from the results from Frontal Range, Colorado, USA, and the Central Loess Plateau, where landslides commonly occur in sparsely vegetated areas. Li et al. (2021) only addressed the relationship between landslide probability and vegetation cover at the regional scale, while excluding the importance of the properties of hillslope materials at a more localized scale. Therefore, we hypothesize that such observations in the study area may not be the result of the mechanical effect of plant roots but may be from the distinctive physical properties and strength of hillslope materials due to differential weathering.

## 3 Materials and methods

### 3.1 Landslide information interpretation

The high resolution GeoEye-1 image (0.5 m × 0.5 m) on October 8, 2013 was orthorectified and the landslide boundary was visually interpreted using ENVI 5.1 and e-Cognition 8. An unmanned aerial vehicle (UAV) was used to obtain a digital elevation model (DEM) with a 5 m resolution. The GeoEye-1 orthographic image and DEM were spatially registered in ArcGIS 10.2 as a standard layer of orthoimage. The landslide initiation condition is represented by the competition between the slope gradient and upslope contribution area ($A-S$):

$$S = kA^{-b} \qquad (1)$$

where $S$ is the local slope (m/m); $A$ is the contribution area above the landslide head scar (m$^2$); $k$ is an empirical constant related to lithology, vegetation, and climate; and $b$ is an empirically defined index.

Field studies were conducted to measure the depth of the head scar and sidewall area using tape, and the failure depth was taken as their average. The landslide volume could then be calculated using the interpreted scar area and failure depth measured. Detailed landside information including the landslide number and area probability, landslide volume and width, head scar and sidewall depth, and the upslope contributing area–slope gradient condition for the south- and north-facing slopes were compared.

### 3.2 Field monitoring and soil sampling

To investigate the hillslope hydrology on south- and north-facing slopes, Frequency Domain Reflectometry (FDR) soil moisture sensors were used in this work to record the volumetric water content. To avoid the randomness of data caused by natural factors such as terrain and vegetation, a total of 16 shallow landslides were investigated to excavate soil profiles and take undisturbed soil samples. Sensors were installed at depths of 30 cm, 70 cm, and 110 cm on the south- and north-facing slopes to monitor the volumetric water content during June and September 2021. Soil moisture monitoring was implemented at two concave sites on the south- and north-facing slopes. The meteorological station was less than 3 km away from the study area to record the rainfall on a 30 min basis. During the sensor installation, undisturbed soil samples near the sensor location were taken for indoor tests, including the dry unit weight, porosity, grain size, shear strength, and hydraulic conductivity. The grain size was analyzed using a Malvern MS 3000 instrument (Malvern, England). In each layer, at least four samples were collected for the consolidated undrained triaxial compression test (CU). Two samples were collected for unsaturated hydraulic conductivity measurement using transient release and imbibition tests (Lu and Godt, 2013). Saturated hydraulic conductivity was determined using the constant water head method (Table 1).

### 3.3 Pore water pressure dissipation

CU tests were performed to obtain the effective cohesion, effective internal friction angle, and pore pressure water dissipation curves. Soil samples with a diameter of 50 mm and height of 100 mm were first saturated in a

vacuum pump. They were then consolidated in the chamber of the GDS apparatus at 50, 100, 150, and 200 kPa confining pressures and 10 kPa backpressure. During each test, the shearing rate was set to 0.1 mm/min, and the device automatically recorded data every 10 s. Owing to the varied particle components and soil texture, the increasing and dissipation ratios varied. This ratio is closely related to the widespread generation of excessive pore-water pressure, which increases the landslide scale. A high excessive pore water pressure, rapid increase ratio, and slow dissipation ratio could cause widespread Coulomb failure within the sliding zone. To demonstrate that the pore water pressure increases or dissipates, the ratio is

$$i = \frac{p_{t+\Delta t} - p_t}{\Delta t} \qquad (2)$$

where $i$ is the increase or dissipation ratio of the excessive pore water pressure, and $p_t$ and $p_{t+\Delta t}$ are the pore water pressures measured during the time interval of $\Delta t$.

### 3.3 Water storage and drainage

The unsaturated permeability of soil mass (diameter 61.8 mm, height 25.4 mm) was measured using the Transient Release and Imbibition method (TRIM) (Lu and Godt, 2013). In this test, the water outflow mass was measured on a 10 min basis. In each test, air pressures of 250 kPa and 0 kPa corresponded to the drying and wetting processes, respectively. The Soil Water Characteristic Curve (SWCC) and Hydraulic Conductivity Function (HCF) were obtained using Hydrus 1-D (Wayllace and Lu, 2012). Using the models proposed by Mualem (1976) and van Genuchten (1980), the constitutive relations between the suction head ($h$), water content ($\theta$), and hydraulic conductivity ($K$) under drying and wetting states can be represented by the following equation:

$$\frac{\theta - \theta_r}{\theta_s - \theta_r} = \left[\frac{1}{1 + (\alpha|h|)^n}\right]^{1-\frac{1}{n}} \qquad (3)$$

and

$$K = K_s \frac{\left\{1 - (\alpha|h|)^{n-1}[1 + (\alpha|h|)^n]^{\frac{1}{n}-1}\right\}^2}{[1 + (\alpha|h|)^n]^{\frac{1}{2}-\frac{1}{2n}}} \qquad (4)$$

where $\theta_r$ is the residual moisture content (%), $\theta_s$ is the saturated moisture content (%), $\alpha$ and $n$ are empirical fitting parameters, $\alpha$ is the inverse of the air-entry pressure head, $n$ is the pore size distribution parameter, and $K_s$ is the saturated hydraulic conductivity (cm/s).

The soil water storage ($S_s$) and drainage ($S_d$) during a rainfall event can be evaluated by the soil depth and the difference between the maximum soil moisture and antecedent soil moisture:

$$S_e = \frac{\theta - \theta_r}{\theta_s - \theta_r} \qquad (5)$$

$$S_s = S_e^w \Delta h \qquad (6)$$

$$S_d = P - S_e^d \Delta h \qquad (7)$$

where $S_e$ is the degree of saturation, $\theta$ is the volumetric moisture content measured (%), $\Delta h$ is the average soil thickness (400 mm in this study), $S_e^w$ and $S_e^d$ are the residual soil moisture in the wetting and drying processes (%), and $P$ is the accumulated rainfall (mm).

### 3.4 Stability fluctuation

In this study, we applied a finite and infinite stability model to assess the slope stability fluctuation during the rainy season as an attempt to examine aspect-dependent landslide initiation from the perspective of classical mechanics and the state of stress (Schmidt et al., 2001). The finite-slope model evaluates the stability $F_s$:

$$F_s = \frac{S_{sr}}{\tau} = \frac{c_l A_l + c_b A_b + A_b(\rho_s - \rho_\omega S_e)\, gz\cos^2\beta \tan\varphi'}{A_b \rho_s gz \sin\beta \cos\beta} \qquad (8)$$

where $\beta$ is the topographic slope angle (°), $A_l$ is the lateral area, m², $A_b$ is the basal area, m², $z$ is the sliding depth (m), $c_l$ is the sum of the effective soil cohesion and the root additional cohesion along the perimeter (kPa),

192     $c_b$ is the basal soil cohesion (kPa), $\rho_s$ is the soil particle density, g/cm$^3$, and $\rho_w$ is the water density, g/cm$^3$.

193     The infinite slope stability model in this study provides insight into the stress variation resulting from changes

194     in the soil suction and water content during infiltration (Lu and Likos, 2006):

195
$$F_s = \frac{\tan \varphi'}{\tan \beta} + \frac{2c'}{\gamma z \sin 2\beta} - \frac{\sigma^s}{\gamma z}(\tan \beta + \cot \beta)\tan \varphi' \qquad (9)$$

196     where $\varphi'$ is the effective friction angle, °; $\beta$ is the topographic slope angle, °; $c'$ is the effective cohesion, kPa; γ

197     is the unit weight of the soil, KN/m$^3$; and $\sigma^s$ is the suction stress (kPa), expressed as:

198
$$\sigma^s = -\frac{S_e}{\alpha}\left(S_e^{n/(1-n)} - 1\right)^{1/n} \qquad (10)$$

199 **4 Results**

200 **4.1 Shallow landslides on south- and north-facing slope**

201     In the study area, the south-facing slope was between 157.5 ° and 247.5 ° and the north-facing slope ranged

202     from 0 ° to 67.5 °, and 292.5 ° to 360 ° (0 ° is the due north). There were 71 shallow landslides on the south-facing

203     slope and 20 landslides on the north-facing slope. Figure 2a shows that shallow landslides on south-facing slopes

204     have larger spatial areas than those on north-facing slopes. Most of the shallow landslides occurred on the south-

205     facing slope (Fig. 2b). The volume of landslides on the south-facing slope was greater than that on the north-facing

206     slope. For landslides on the south-facing slope, the basal area was 372.64 m$^2$ and the width was 14.9 m on average.

207     For landslides on the north-facing slope, the average basal area was 157.28 m$^2$ and the width was 7.7 m (Fig. 2c).

208     Although the landslides on the south-facing slope had a larger volume and greater width, the depth of the head-scar

209     and sidewall area are no greater than those on the north-facing slope. Field studies showed that the averaged depth

210     for landslides on the north-facing slope was 1.02 m, which was deeper than the depth of 0.83 m for landslides on

211     south-facing slope (Fig. 2d). The landslides on the south-facing slope exhibited an overwhelming propensity for

212     occurrence in terms of number and area. Meanwhile, the failure depth was no more than that of the landslides on the

213     north-facing slope.

214     Shallow landslides can be modeled as occurring when sufficient through-flow converges from the upslope

215     contribution area to the hollow area and triggers slope instability (Montgomery and Dietrich, 1994). Their

216     topographic initiation conditions are controlled by the spatial competition between the slope and upslope contribution

217     being area dependent (Stock and Dietrich 2003 and 2006; Horton et al., 2008). For the shallow landslides in the

218     study area, the averaged upslope contributing area and slope gradient did not significantly differ (Fig. 3a). Meanwhile,

219     the lower limit line representing the minimum initiation condition for landslides on south-facing slopes was lower

220     than that on the north-facing slopes (Fig. 3b). This indicates that a higher upslope contribution area was required to

221     provide sufficient through-flow conditions and trigger slope failures on the north-facing slope. Given that the

222     landslides in the study area were triggered by prolonged antecedent precipitation and intensive rainfall (Li et al.,

223     2021), sufficient rainfall infiltration could result in a high soil water content within the displaced mass, leading to a

224     decrease in matric suction and soil strength. The generation of pore pressure in response to intense rainfall also plays

225     an important role in shallow landslides. Therefore, we have proposed two assumptions to elucidate the distribution

226     and scale of aspect-dependent landslides. The first assumption is that the basal area of the landslide may be related

227     to the soil strength and high pore-water pressure. This assumption can be tested by the pore water properties,

228     including the pore water generation potential and dissipation ratio during the failure process. The second assumption

229     is that the south-facing slope may have a higher failure potential than the north-facing slope in a given rainfall process.

230     This can be determined from the stability comparison using equations (8) and (9).
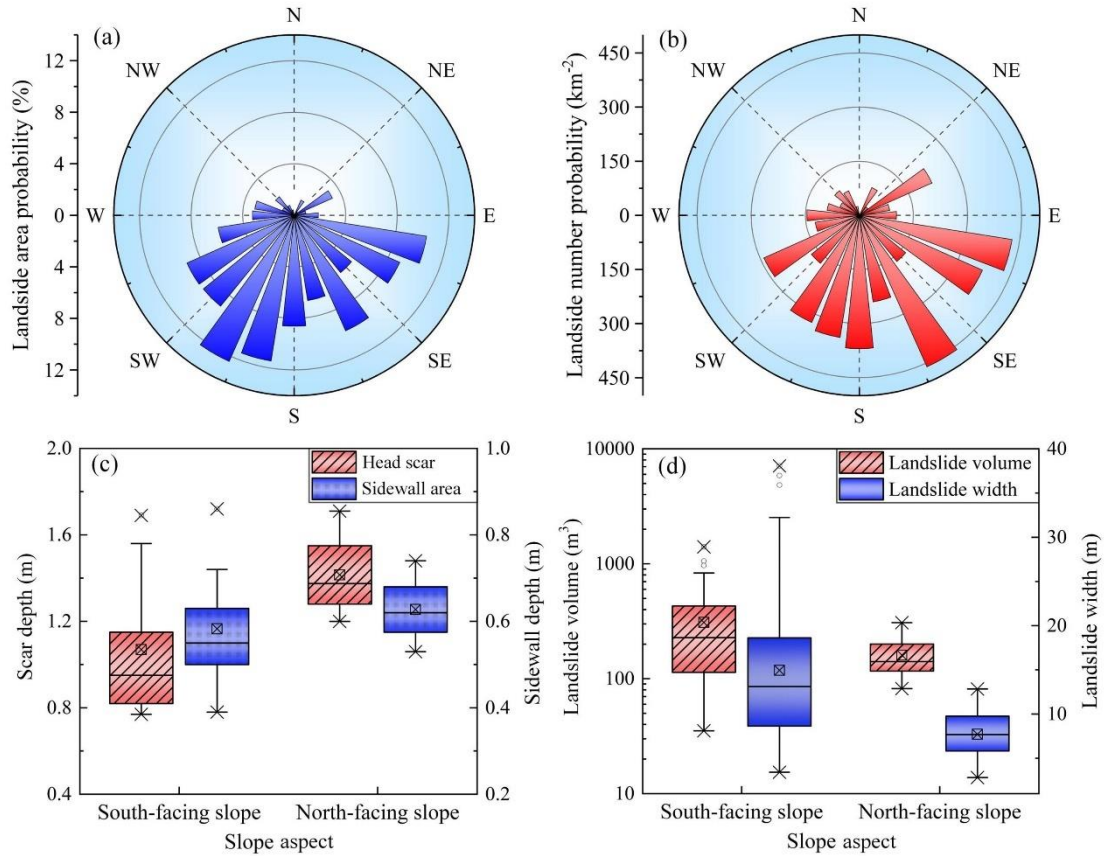
231

232 **Fig. 2.** Spatial distribution and geometric characteristics of the landslide: (a) Landslide area probability vs slope

233 aspect; (b) landslide number probability vs slope aspect; (c) landslide volume and width vs slope aspect; (d)

234 scar depth and sidewall depth vs slope aspect. The edge line of "box" in the box chart shows the 75th quantile,

235 median and 25th quantile from top to bottom. The length of the box is referred to as the inter-quartile distance.

236 The crossed square inside the box is the average value. The whiskers extend to the maximum and minimum

237 values except the outliers. The circles are the outliers, and the cross symbol is the maximum and minimum

238 values for all the data.
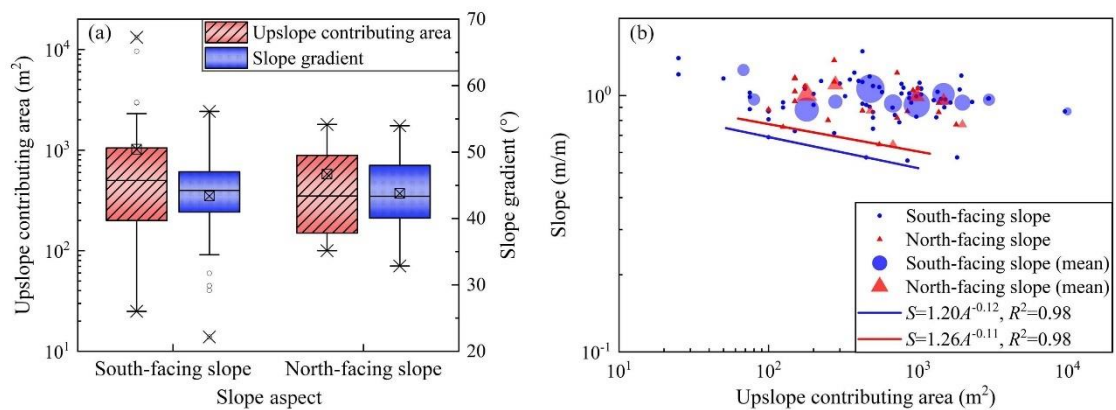
239

240 **Fig. 3.** Upslope contributing area and slope gradient condition: (a) Upslope contribution area and mean slope vs

241 slope aspect; and (b) the upslope contributing area vs mean slope gradient above the landslide area. The large

242 icons are the average value with the radius size proportional to the number of landslides. The small icons

243 represent all the individual data values.

244 **4.2 Differences in soil physical properties**

245 To show the differences in the physical properties of the hillslope materials, the dry unit weights, porosity, and

246 grain size distribution of the soil mass in the three layers on each slope were compared (Fig. 4). The effective
247 cohesion and inner friction angle were then examined with respect to the particle component (Table 1 and Fig. 5).
248
249 Table 1 Physical properties and strength parameters of the soil mass

| Parameters | South-facing slope | | | North-facing slope | | |
|---|---|---|---|---|---|---|
| | Layer 1 | Layer 2 | Layer 3 | Layer 1 | Layer 2 | Layer 3 |
| Unit weight of soil (kN/m$^3$) | 14.8 | 15.6 | 17.2 | 14 | 16.6 | 17.1 |
| Porosity (%) | 43.0 | 43.1 | 36.2 | 42.5 | 37.3 | 36.4 |
| Effective cohesion (kPa) | 6.5 | 17.5 | 21.2 | 5.3 | 9.1 | 7.9 |
| Effective inner friction angle (°) | 29.8 | 25 | 31 | 27.1 | 35.2 | 41 |
| Saturated hydraulic conductivity (cm/s) | $6.4\times10^{-3}$ | $6.2\times10^{-4}$ | $4.4\times10^{-4}$ | $8.8\times10^{-3}$ | $1.2\times10^{-3}$ | $4.3\times10^{-3}$ |
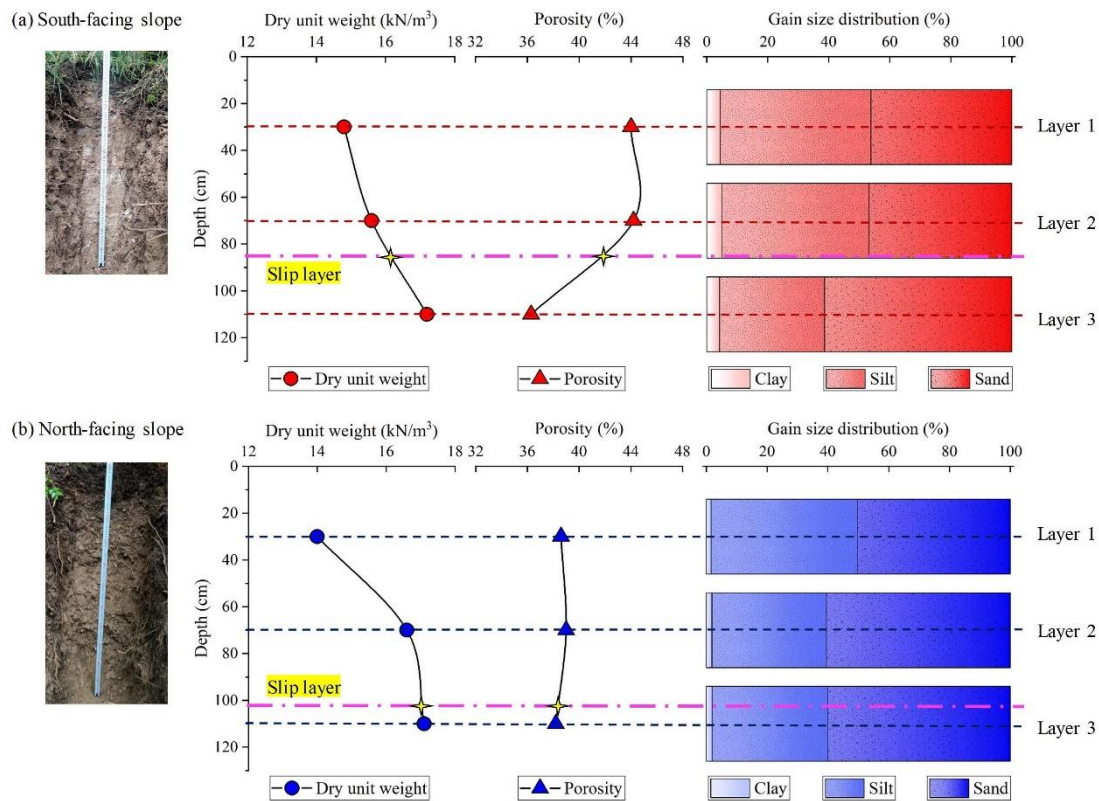
250
251 **Fig. 4.** Differences in the soil properties including dry unit weights, porosity, and grain size in sand, silt, and clay.
252   (a) Physical properties of soil mass on the south-facing slope; and (b) physical properties of soil mass on the
253   north-facing slope. The two-soil profile photos were taken by Yanglin Guo during field studies.
254
255   For the soil mass on the south-facing slope, the dry unit weights increased with soil depth, whereas the porosity
256 and saturated hydraulic conductivity decreased (Fig. 4a and Table 1). For Soil layers 1 and 2, the soil textures were
257 similar, because the proportions of sand, silt, and clay did not differ significantly. However, the proportion of silt in
258 Soil layer No. 3 was no more than that in layers No. 1 and 2, and the sand proportion was higher. The average failure
259 depth was above Soil Layer No. 3 and below Soil Layer No. 2. For the soil mass on the north-facing slope, the dry
260 unit weight also increased with soil depth. Unlike the south-facing slope, the porosity of the soil mass for the three
261 soil layers was approximately 38% and did not differ among them. For the soil texture, the proportion of sand in Soil

Layer No. 1 was no more than that in Soil Layers No. 2 and 3 (Fig. 4b). The depth of the failure plane was close to that of Soil Layer 3.

In comparison, one of the main difference was the higher saturated hydraulic conductivity for the soil mass above the failure plane on the north-facing slope. This may have resulted from the high porosity and sand proportion. This indicates that the rainfall infiltration on the north-facing slope could penetrate faster than that of the south-facing slope. The soil mass of the three layers on the south-facing slope had a higher proportion of fine particles than those on the north-facing slope if gravel was considered (Fig. 5). The saturated hydraulic conductivity for the soil masses from Soil Layers No. 2 and 3 on the south-facing slope was lower than that on the north-facing slope. This is expected because the porosity and proportion of fines on the south-facing slope were higher.
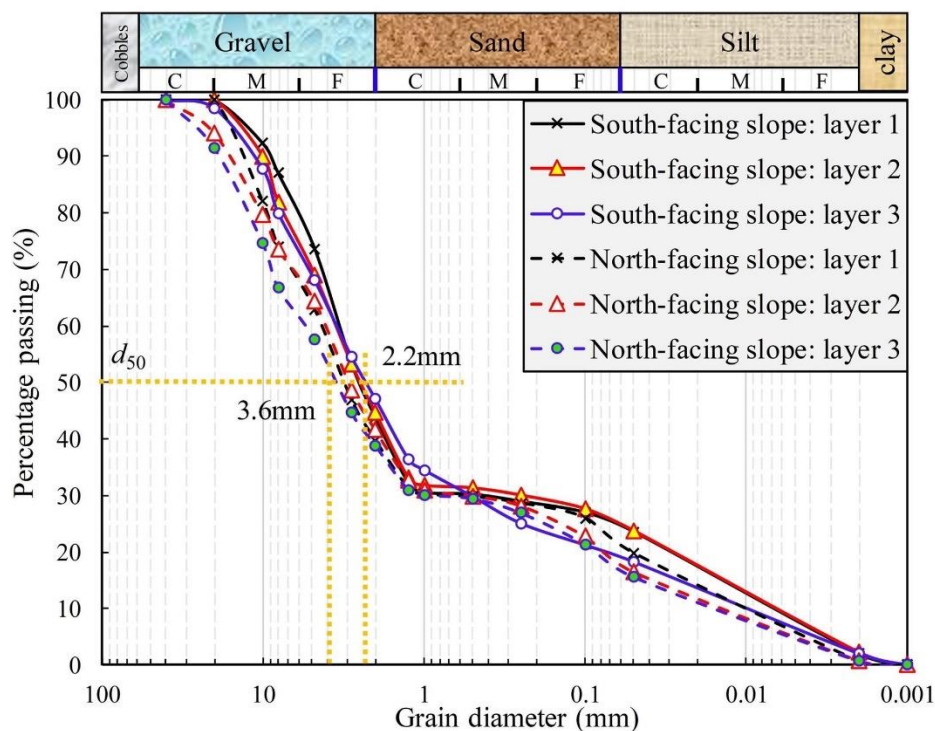
**Fig. 5.** Soil particle component curves

According to the results of the triaxial shear test (Table 1), the soil mass in each layer on the north-facing slope had a smaller effective cohesion than that on the south-facing slope. The effective cohesion on the failure plane for landslides on the south-facing slope may be twice that on the north-facing slope. However, the effective inner friction angles for the soil masses of Soil Layers 2 and 3 on the north-facing slope were far greater than those on the south-facing slope. These differences in effective cohesion and inner frictional angle may be attributed to the higher clay and silt and fewer coarse grains within the soil mass on the south-facing slope.

### 4.3 Pore water pressure properties

The consolidation module of the triaxial shear test was used to measure the generation and dissipation process of the pore water pressure. The principle is to consolidate and drain soil from the initial saturated state. Under the same confining pressure, there are pronounced differences in the consolidation rate, consolidation time, and peak rise in pore water pressure for different soil properties. The results of the pore water pressure during the consolidation process under 200 kPa effective confining pressure were taken here (Fig. 6). The peak value of pore water pressure within the soil mass on the south-facing slope was higher than that on the north-facing slope. The peak value of the pore water pressure within the soil mass on the south-facing slope increased to 150–200 kPa. However, the peak value of pore water pressure within the soil mass on the north-facing slope was below 150 kPa. Both the rising and decaying rates of pore water pressure for Soil Mass layers 1 and 2 on the south-facing slope were lower than those

289  on the north-facing slope. The rate and decaying rates for Soil Mass layer No. 2 on the south-facing slope were 1.2
290  kPa/10 s and −0.031 kPa/10 s, respectively. However, they were 9.6 kPa/10 s and −0.765 kPa/10 s for the soil mass
291  on the north-facing slope.
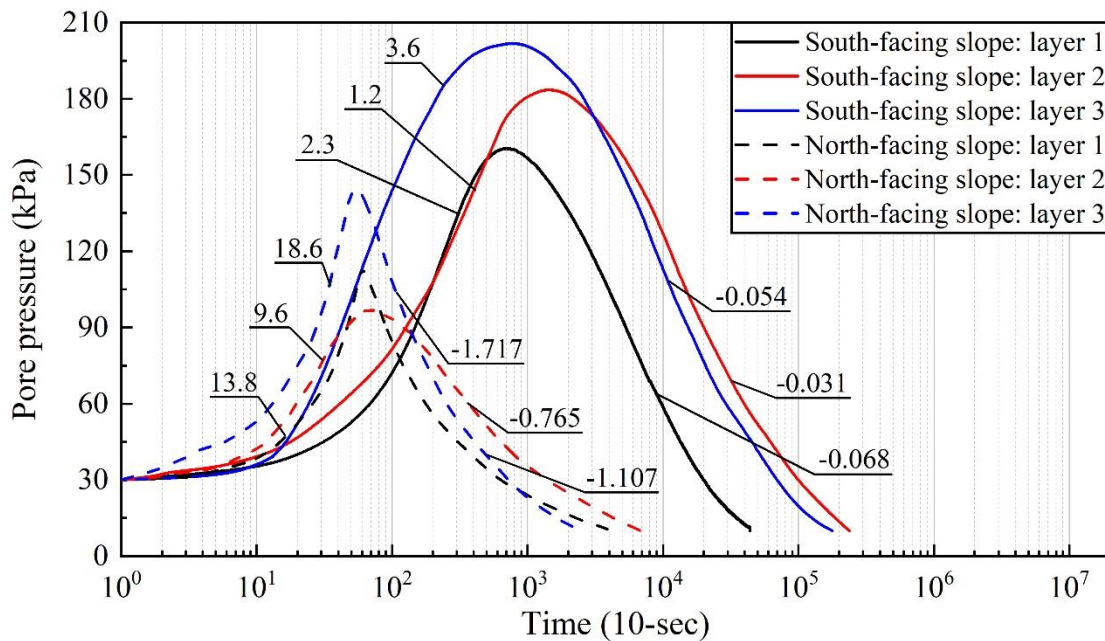
292

293  **Fig. 6.** Variation in pore water pressure under effective confining pressure of 200 kPa by GDS triaxial shear tests.

294

295      The lower peak pore water pressure demonstrates the effect of fine particles on the pore water pressure, which
296  directly affects landslide mobility and scale. Rainfall-induced landslides result from an increase in positive pore
297  water pressure within the failure plane, which reduces the effective stress and shear strength of the soil (Terzaghi,
298  1950). This often occurs in the undrained soil layer, which can easily cause slope liquefaction (Sassa, 1984). The
299  increase in pore water pressure predominantly depends on the speed of landslide movement, soil deformation, and
300  soil permeability. If the shear rate is given, the dissipation rate of pore water pressure for high-permeability soil is
301  faster, and therefore, the increase in pore pressure is smaller (Iverson and LaHusen, 1989; Iverson et al., 1997). As
302  shown in Table 1, the saturated hydraulic conductivity for Soil Mass Layers No. 2 and 3 on the north-facing slope
303  was 10 times that of the south-facing slope. Therefore, the peak pore water pressure measured during the test for the
304  soil mass on the south-facing slope was smaller. The soil mass on the north-facing slope had higher sand and gravel
305  contents than that on the south-facing slope (Fig. 5). A high clay content on the south-facing slope filled the
306  macropores within the soil mass and reduced the pore water discharge rate. Wang and Sassa (2003) found that fine
307  particles play the most important role in the dissipation of pore pressure. The pore water pressure within the saturated
308  sand increased with shear rate. The soil mass with high coarse particles produced less pore water pressure than the
309  soil with high fine particles during the shear process. Therefore, the high permeability of the soil mass on the south-
310  facing slope may result in low peak pore water pressure. The higher fine particles may result in a slow increase and
311  dissipation of the pore water pressure. This slow pore water pressure dissipation could result in the liquefaction
312  failure of the sliding mass and a larger landslide area.

313  **4.4 Unsaturated hydraulic conductivity**

314      4.4.1 Measured water outflow mass

315      Figure 7 shows the water outflow mass measured for a given 10 min period during the drying and wetting
316  processes. The water outflow masses measured for Soil Layers 2 and 3 on the north-facing slope were generally
317  higher than those on the south-facing slope. For the drying tests using the soil mass of Soil Layers No. 2 and 3 on

the north-facing slope, the given water outflow masses were 0.102 g/10 min and 0.131 g/10 min, respectively. However, the water outflow masses measured for the soil mass of Soil Layers No. 2 and 3 were 0.077 g/10 min and 0.050 g/10 min, respectively, on the south-facing slope (Fig. 7a). For tests using the same layers of the soil mass in the wetting process, the water outflow masses measured were 0.051 g/10 min and 0.094 g/10 min on the north-facing slope, respectively, and 0.032 g/10 min and 0.027 g/10 min, respectively, on the south-facing slope (Fig. 7b). Overall, the permeability of the soil mass on the north-facing slope was higher than that on the south-facing slope. The same results were obtained when the saturated hydraulic conductivities of the soil layers were measured using the constant water head method (Table 1).
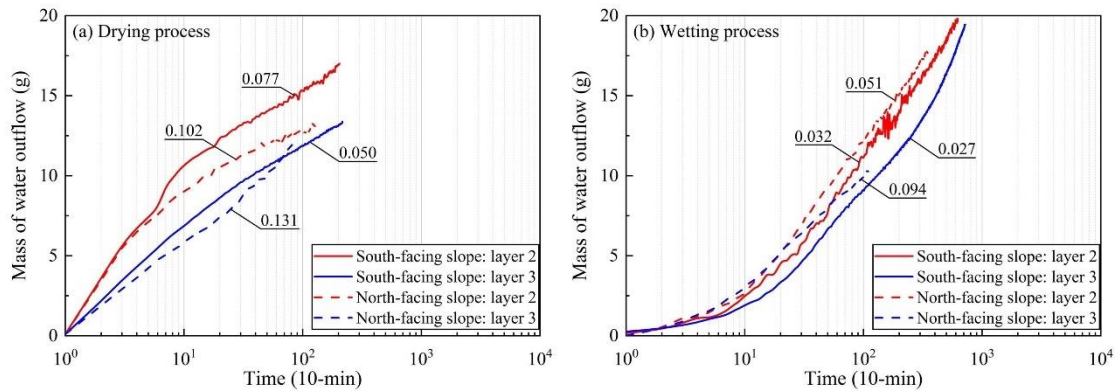
**Fig. 7.** Mass of water outflow during the drying and wetting process: (a) drying tests, (b) wetting tests
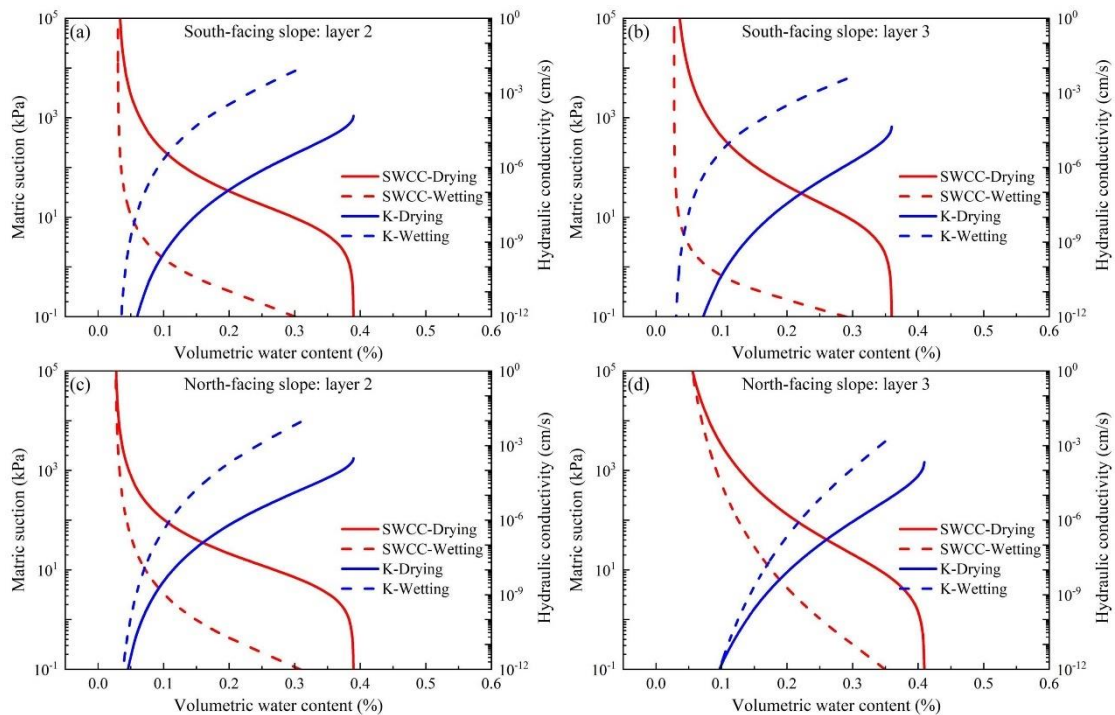
**Fig. 8.** Soil water curve obtained using the TRIM test: (a) Layer No. 2 on the south-facing slope, (b) Layer No. 3 on the south-facing slope, (c) Layer No. 2 on the north-facing slope, and (d) Layer No. 3 on the north-facing slope.

### 4.4.2 SWCC and HCF curves

Hydraulic properties such as the Soil Water Characteristic Curve (SWCC) and Hydraulic Conductivity Function (HCF), are critical for the analysis of water flow movement and mechanical behavior of unsaturated soil material. In this study, the Transient Release and Imbibition Method (TRIM) for unsaturated hydraulic property measurement.

The advantage of the TRIM method is that it combines physical and numerical experiments. It employs a relatively simple and reliable measurement of transient water content using an electronic balance to record the signature of transient unsaturated flow. It also takes advantage of the robust inverse modeling capability to simulate the physical process. The apparatus could accommodate both undisturbed and remolded samples. The results of this study were obtained using the Hydrus-1D code with the reverse modeling option, and the Levenberg–Marquardt non-linear optimization algorithm. This minimized the error between the results of the test and the simulation (Wayllace and Lu, 2012). Meanwhile, to ensure the uniqueness of the parameters, the algorithm repeatedly runs with different initial parameter estimates until it converges to obtain the same or similar results. The prediction results are then compared with the function curves of water flow and time obtained from the actual experiment so that they can be combined to meet certain accuracy requirements. In this experiment, the R square of the regression between the optimized predicted value and the observed value was greater than 0.99. The model constraint effect of the TRIM under two suction increment steps was better, and the parameters obtained by the inversion calculation were more accurate (Lu and Godt, 2013). Table 2 shows the soil parameters obtained using the Hydrus 1-D inversion.

Using these parameters, the SWCC and HCF curves of the soil mass at Soil Layers 2 and 3 on the north- and south-facing slopes can be drawn (Fig. 8). Air-entry pressure and residual water content are two important parameters that describe the hydrological and mechanical characteristics of the hillslope materials. The air-entry pressure represents the critical value at which air enters the saturated soil and starts to drain. For Soil Layer No. 2, the difference between the air entry values of the north- and south-facing slopes can reach 14.03 kPa (Figs. 8a and 8c). The residual water content and air-entry pressure of the south-facing slope were higher than those of the north-facing slope. For Soil Layer No. 3, the soil mass on the north-facing slope has the smallest air-entry pressure, which is 0.51 times that of the air-entry pressure of the south-facing slope (Figs. 8b and 8d). The saturated hydraulic conductivities of Soil Layers No. 2 and 3 on the south-facing slope were lower than those on the north-facing slope in both the drying and wetting processes. The saturated hydraulic conductivity of the soil mass on the north-facing slope in the wetting test was one order of magnitude higher than that on the south-facing slope. These results suggest that it is more difficult for the soil mass to absorb and drain water than the soil mass on the north-facing slope.

Table 2 Parameters describing the Soil and Water Characteristic Curve (SWCC) and the Hydraulic Conductivity Function (HCF) from Hydrus 1-D

| Parameters | Definition | South-facing slope | | North-facing slope | |
|---|---|---|---|---|---|
| | | Layer 2 | Layer 3 | Layer 2 | Layer 3 |
| $\theta_r$ | Residual moisture | 0.0302 | 0.0278 | 0.0262 | 0.0268 |
| $\theta_s^d$ | Saturated moisture | 0.39 | 0.36 | 0.39 | 0.41 |
| $\theta_s^w$ | | 0.36 | 0.38 | 0.39 | 0.42 |
| $\alpha^d$ (kPa$^{-1}$) | The inverse of the air-entry pressure head | 0.0128 | 0.0117 | 0.0156 | 0.0141 |
| $\alpha^w$ (kPa$^{-1}$) | | 0.78 | 0.94 | 1.21 | 1.86 |
| $n^d$ | The pore size distribution parameter | 1.49 | 1.39 | 1.57 | 1.27 |
| $n^w$ | | 1.63 | 1.85 | 1.43 | 1.18 |
| $K_s^d$ (cm/s) | Saturated hydraulic conductivity | $1.52\times10^{-4}$ | $0.64\times10^{-4}$ | $3.76\times10^{-4}$ | $4.56\times10^{-4}$ |
| $K_s^w$ (cm/s) | | $9.58\times10^{-2}$ | $4.93\times10^{-2}$ | $4.10\times10^{-1}$ | $4.68\times10^{-1}$ |

Notes: the superscript $d$ and $w$ indicate drying and wetting states.

## 4.5 Water storage and drainage

To show the water storage during the rainfall process and the water drainage after the rainfall, the timely recorded soil moisture at various soil layers and the rainfall process during June 11 and August 20 were used (Figs. 9a and 9b). In comparison, this is likely the most important finding, as it shows that the soil becomes nearly saturated on the south slope, but not on the north slope. This implies that the soil water on the south-facing slope has difficulty in draining because of the presence of more fine grains and slow pore water pressure dissipation. The stable soil moisture from Soil Layers No. 2 and 3 for both slopes may be attributed to the long dry seasons in the study area. The daily rainfall amount > 30 mm on July 9 and 23 resulted in an increase in soil moisture for all the slope layers.
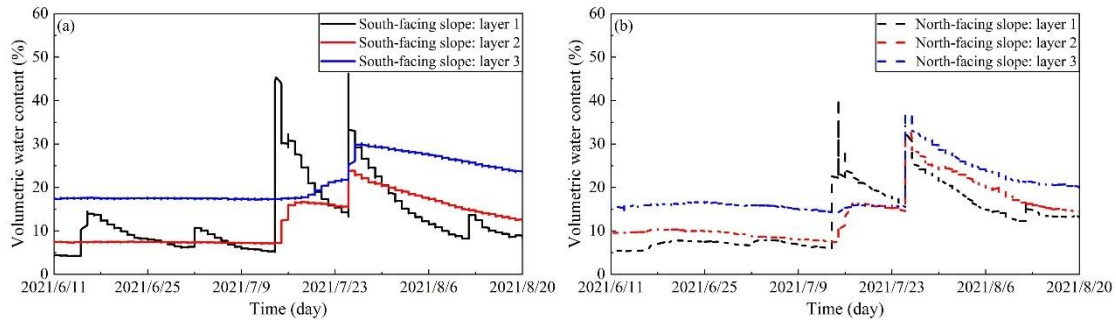
**Fig. 9.** Field monitored volumetric water content: (a) Soil moisture on the south-facing slope, and (b) soil moisture on the north-facing slope.
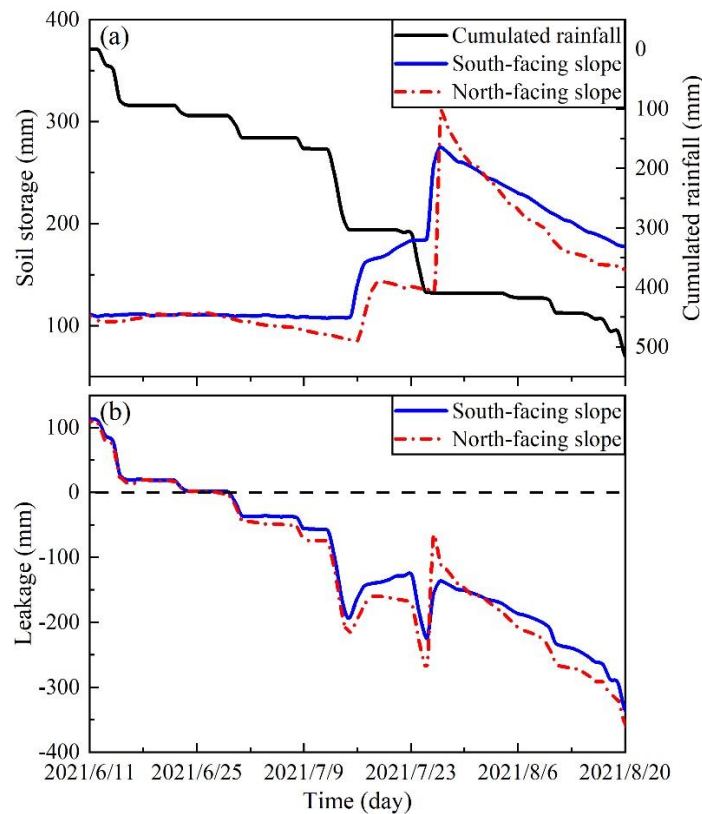
**Fig. 10.** Seepage model of slope water storage and drainage. (a) soil water storage, (b) soil water drainage

Figure10a shows that the storied water of the north- and south-facing slopes did not synchronously increase with accumulated precipitation. When the storied water rapidly increased, the increase in soil water storage of the north-facing slope was greater than that of the south-facing slope. On July 26, a rainfall of 30.8 mm/h was recorded,

383   and the water storage of the slope reached the peak. The peak of the water storage on the north-facing slope was

384   higher than that of the south-facing slope. However, when the accumulated rainfall tends to be stable, that is, when

385   the rainfall stops for a period of time, the decline rate of the soil water storage on the north-facing slope is

386   substantially higher than that on the south-facing slope. The soil water storage of the south-facing slope was always

387   higher than that of the north-facing slope during rainfall. During the drainage process, the seepage rate of the north-

388   facing slope was greater than that of the south-facing slope (Fig. 10b). Therefore, the south-facing slope had a better

389   water storage performance, and the north-facing slope had a higher drainage performance.

390   **4.6 Stability fluctuation**

391   In this study, the infinite slope model and the finite slope model were used to characterize the sensitivity of

392   landslide triggering to determine the main mechanism of high landslide probability on south-facing slopes. The

393   infinite slope model can be used to examine the transient stress changes caused by water entering the soil,

394   emphasizing the differences in soil permeability (Lu and Likos, 2006; Lu and Godt, 2013). The finite slope model

395   focuses on the cohesion of the base surface and lateral periphery of the ground landslide source body, as well as the

396   influence of the additional lateral cohesion provided by the vegetation root system for the landslide (Schmidt et al.,

397   2001; Dai et al., 2022).
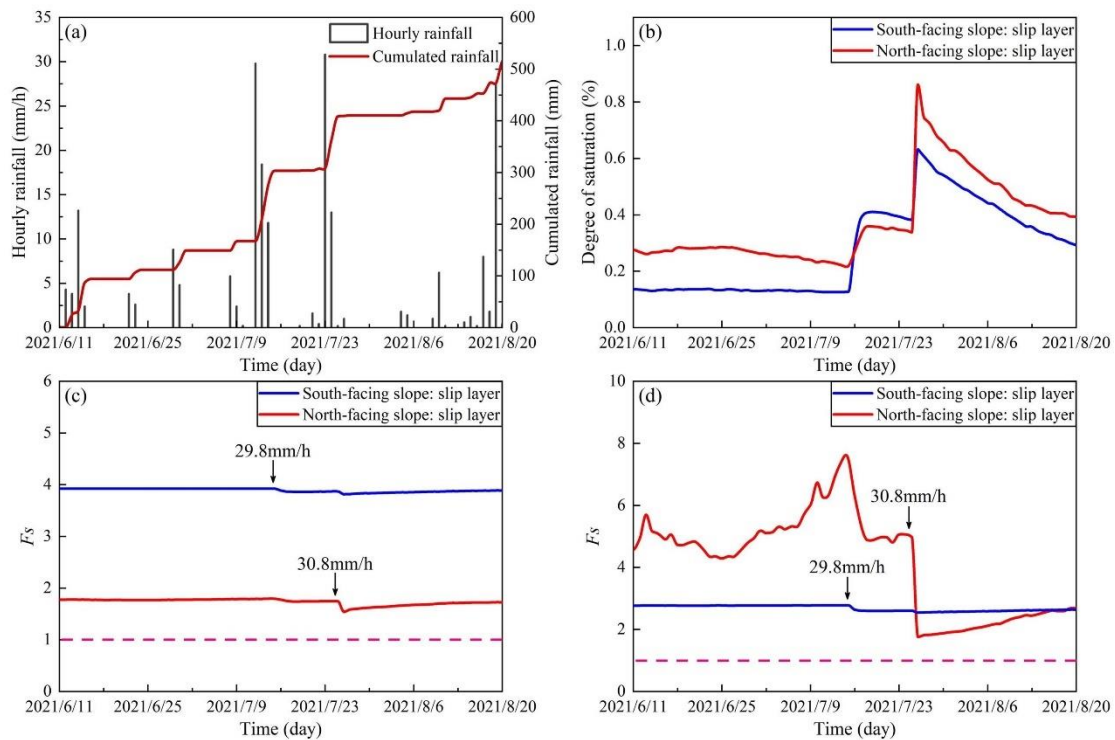
399   **Fig. 11.** Change in slope stability fluctuation: (a) rainfall records, (b) degree of saturation, (c) stability of finite slope

400   model, and (d) stability of infinite slope model.

401

402   Figure 11a shows the rainfall records from June 11 to August 20, 2021. In general, the degree of saturation of

403   the sliding layer on the south-facing slope was higher than that on the north-facing slope (Fig. 11b). In the finite

404   model, the stability of the south-facing slope was always higher than that of the north-facing slope (Fig. 11c). In the

405   infinite model, the stability of the north-facing slope was generally higher than that of the south-facing slope, and

406   the stability of the north-facing slope fluctuated substantially (Fig. 11d). On July 26, a rainfall event with a maximum

407   intensity of 30.8 mm/h resulted in a sudden decrease in stability. The estimated stability index of the north-facing

408   slope decreased to become lower than that of the south-facing slope and then increased afterwards. Although the soil

409   moisture of the south-facing slope increased substantially during the rainfall event on July 16, the stability fluctuation

410 was relatively small. This may be related to the relatively strong effective cohesion and smaller pore structure.
411 Overall, the results of the finite slope model have shown that the south-facing slope has a relatively high stability.
412 This is predominantly attributed to the effective cohesion of hillslope materials on the south-facing slope being
413 stronger than that of the north-facing slope although the basal area of the landslide is more than double. However,
414 this result is inconsistent with the high landslide density on the south-facing slope. Considering the soil parameters
415 of the soil moisture curve, the results of the infinite slope model have shown that the north-facing slope showed a
416 higher level of stability. In the analysis of finite and infinite models, the stability fluctuation amplitude of the south-
417 facing hillslope was smaller than that of the north-facing hillslope This indicated that the water movement on the
418 south-facing slope was less active than that of the north-facing slope. Therefore, in the study area, the change in soil
419 stress was more sensitive to slope stability than the change in root soil cohesion. The change in soil permeability
420 caused by differential weathering of the bedrock could be responsible for aspect-dependent landslide initiation in the
421 study area.

## 5 Discussion

423 The strong propensity for landslides in some arid environments in the Northern Hemisphere is scientifically
424 interesting, and some researchers have highlighted the contribution of plant roots. This finding is to be expected in
425 the future in other mountain regions, where water is a limiting factor for local system sustainability. In the Colorado
426 Frontal range, McGuire et al. (2016) found that the apparent cohesion supplied by roots was responsible for the
427 connection observed between landslide distribution and slope aspect (Ebel, 2015; Rengers et al., 2016). In the study
428 area, Li et al. (2021) also found that plant roots may explain the connection observed between vegetation cover and
429 landslide probability for the entire study area. Dai et al. (2022) found that a strong root network and high saturated
430 hydraulic conductivity may promote the $A-S$ condition of shallow landslides. On the Loess Plateau in China, some
431 researchers have observed that the strong propensity for shallow landslide initiation is closely related to the present-
432 day tree density, and plant roots do not penetrate over the failure plane (Guo et al., 2020; Deng et al., 2022). However,
433 the strong propensity for shallow landslides on north- and south-facing slopes cannot be attributed to plant roots,
434 because the artificial vegetation on both slopes is the same. Conversely, these observations could be the result of the
435 soil hydraulic and mechanical properties from differential weathering.

436 This study has contributed to knowledge of the effect of differential weathering on aspect-dependent landslide
437 initiation from the perspective of soil hydraulic properties, in addition to the mechanical and hydrological effects of
438 plant roots. Except for the strong propensity for a high number of landslides, shallow landslides on south-facing
439 slopes have exhibited larger areas and greater widths than those on the north-facing slopes (Fig. 2). The effective
440 cohesion of the failure zone on the south-facing slope was stronger than that on the north-facing slope. The basal
441 area of shallow landslides in the study area may be attributed to effective cohesion, because some statistical results
442 have shown that incoherent materials favor shallow landslides with no limitation in size. Meanwhile, cohesive
443 materials favor deep landslides and show a limitation for small sizes (Larsen et al., 2010; Frattini and Crosta, 2013;
444 Milledge et al., 2014). However, a stronger effective cohesion tends to promote the $A-S$ conditions of shallow
445 landslides. A larger up-slope contributing area or steeper gradient is required to trigger slope failure. Figure 3 shows
446 that some shallow landslides on south-facing slopes fail at lower upslope contributing areas. Therefore, soil hydraulic
447 property-related factors, such as the rising or dissipation of pore water pressure, water storage, and drainage, may
448 contribute to the phenomena observed.

449 The saturated hydraulic conductivities obtained by the constant water head and TRIM methods coincide, which
450 demonstrates that the hillslope material on the north-facing slope has a larger water infiltration (Tables 1 and 2).
451 However, the results of the stability analysis using the finite and infinite models imply that the failure potential of
452 slides on a north-facing slope is lower than that on a south-facing slope, although the stability index fluctuates more

heavily than the north-facing slope. These differences imply that slope failures on a north-facing slope may only occur under intensive rainfall conditions or by a combination of prolonged antecedent precipitation and short duration intensive rainfall. For potential failures on south-facing slopes, the combination of prolonged antecedent precipitation and short duration intensive rainfall should be a potential trigger owing to the low hydraulic conductivity and pore water pressure dissipation. This study highlights the role of hydraulic properties in landslide occurrence. Although the south- and north-facing slopes are underlain by granite, the physical properties of hillslope materials such as excessive pore water pressure, strength of sliding mass, soil water storage, and leakage are significantly different. This finding cannot be random because the study area has been selected on the condition that it is relatively far from the northern and eastern areas where local soils are predominantly loess deposits, and the study areas of Li et al. (2021) and Dai (2022), where the bedrock underneath differs substantially. The main purpose of this work is to elucidate the reason for aspect-dependent landslide initiation from the perspective of soil hydraulic properties. These differences result from differential weathering owing to the amount of direct sunlight. Other mechanics such as numerical or relative dating methods and preferential flow in the macropore distribution could provide new evidence for such observations.

**6 Conclusion**

Previous research on the strong propensity for shallow landslides on south-facing slopes over north-facing slopes has highlighted the role of plant roots. In a localized area with the same vegetation including plant roots, they do not penetrate the failure layer. These observations cannot be attributed to plant roots and may result from the differential weathering of bedrock under the influence of hydrothermal conditions. In this study, we jointly explained the influence of bedrock weathering on soil hydraulic properties from physical and mechanical properties, pore water pressure, unsaturated hydraulic conductivity, water storage and drainage, and slope stability fluctuation during monitoring, and studied landslide initiation related to slope direction. The following conclusions were drawn:

(1) In terms of soil physical and mechanical properties on both slopes, the soil masses on the south-facing slope were rich in clay content, whereas the soil mass on the north-facing slope had relatively high sand content. The effective cohesion of the soil mass on the south-facing slope was higher than that on the north-facing slope, while the effective frictional angle was smaller.

(2) The results of the GDS tests showed that the dissipation rate of pore water pressure for soil mass on the south-facing slope was substantially lower than that on the north-facing slope. Higher effective cohesion and slower pore water pressure dissipation may result in a larger basal area for shallow landslides on south-facing slopes.

(3) The soil mass on the south-facing slope had a higher residual water content and air entry pressure, and a lower saturated hydraulic conductivity than that of the north-facing slope. For water storage and drainage performance, the storied water from the south-facing slope was higher than that of the north-facing slope, while the north-facing slope had a higher leakage rate. The results of the stability analysis based on the finite and infinite models show that the infinite slope model may be suitable for elucidating aspect-dependent landslide distribution in the study area.

**Acknowledgements**

This study was supported by the Fundamental Research Funds for the Central Universities (Grant No. 2018BLCB03), the State Key Program of National Natural Science of China (Grant No. 42130701), and the National Nature Science Foundation of China (42177309). The authors sincerely thank the contributions of other colleges, including Muyang Li, Zhisheng Dai, Lv Miao, Lijuan Wang, and Jiayong Deng, for their previous work near the study area.

**Code/Data availability**

The raw/processed data in this work cannot be shared at this time, because the data also form part of an ongoing

495 study.

**Author contributions**

497 Professor Ma Chao found a strong propensity for shallow landslide initiation on south-facing hillslopes in the study
498 area and launched a research proposal. Miss Yanglin Guo completed the sampling collection and indoor tests.

**Competing interests**

500 All authors have declared that there were no conflicts of interests and competing interests.

**References**

502 [1]   Bierman, P. R., Montgomery, D. R.: Key Concepts in Geomorphology, W.H. Freeman, 2014.

503 [2]   Birkeland, P. W.: Soils and Geomorphology, New York: Oxford University Press, 1999.

504 [3]   Bogaard, T. A., Greco, R.: Landslide hydrology: from hydrology to pore pressure, Wiley Interdiscip. Rev.
505       Water, 3, 439-459, https://doi.org/10.1002/wat2.1126, 2016.

506 [4]   Coe, J. A., Kean, J. W., Godt, J. W., Baum, R. L., Jones, E. S., Gochis, D. J., Anderson, G. S.: New insights
507       into debris-flow hazards from an extraordinary event in the Colorado front range, GSA Today, 24, 4-10,
508       https://doi.org/10.1130/GSATG214A.1, 2014.

509 [5]   Dai, Z. S., Ma, C., Miao, L., Li, M. Y., Wu, J. L. and Wang, X. H.: Initiation conditions of shallow landslides
510       in two man-made forests and back estimation of the possible rainfall threshold, Landslides, 19, 1031-1044,
511       https://doi.org/10.1007/s10346-021-01823-1, 2022.

512 [6]   Deng, J. Y., Ma, C., and Zhang, Y.: Shallow landslide characteristics and its response to vegetation by example
513       of July 2013, extreme rainstorm, Central Loess Plateau, China. Bulletin of Engineering Geology and the
514       Environment, 81-100, https://doi.org/10.1007/s10064-022-02606-1, 2022.

515 [7]   Ebel, B. A., Rengers, F. K., Tucker, G. E.: Aspect-dependent soil saturation and insight into debris-flow
516       initiation during extreme rainfall in the Colorado front range, Geology, 43, 659-662,
517       https://doi.org/10.1130/G36741.1, 2015.

518 [8]   Frattini, P., Crosta, G. B.: The role of material properties and landscape morphology on landslide size
519       distributions, Earth Planet. Sci. Lett., 361, 310-319, https://doi.org/10.1016/j.epsl.2012.10.029, 2013.

520 [9]   Fu, B. J., Wang, Y. F., Lu, Y. H., He, C. S., Chen, L. D., Song, C. J.: The effects of land-use combinations on
521       soil erosion: a case study in the Loess Plateau of China, Prog. Phys. Geo., 33, 793-804,
522       https://doi.org/10.1177/0309133309350264, 2009.

523 [10]  Fu, B. P.: Mountain climate, Science Press, 1983 (in Chinese)

524 [11]  Geroy, I. J., Gribb, M. M., Marshall, H. P., Chandler, D. G., Benner, S. G., McNamara, J. P.: Aspect influences
525       on soil water retention and storage, Hydrological Processes, 25, 3836-3842, https://doi.org/10.1002/hyp.8281,
526       2011.

527 [12]  Godt, J. W., Baum, R. L., and Lu, N.: Landsliding in partially saturated materials. Geophys. Res. Lett., 36,
528       L02403, https://doi.org/10.1029/2008GL035996, 2009.

529 [13]  Guo, F. Y., Meng, X. Y., Li, Z. H., Xie, Z. T., Chen, G., He, Y. F.: Characteristics and causes of assembled
530       geo-hazards induced by the rainstorm on 25th July 2013 in Tianshui City, Gansu, China, Mt. Res., 33, 100-
531       107, 2015 (in Chinese)

532 [14]  Guo, W. Z., Chen, Z. X., Wang, W. L., Gao, W. W., Guo, M. M., Kang, H. L., Li, P. F., Wang, W. X., Zhao,
533       M.: Telling a different story: The promote role of vegetation in the initiation of shallow landslides during
534       rainfall on the Chinese Loess Plateau, Geomorphology, 350, 106879,
535       https://doi.org/10.1016/j.geomorph.2019.106879, 2020.

[15] Hungr, O., McDougall, S., Bovis, M.: Entrainment of material by debris flows. In: Debris-flow Hazards and Related Phenomena. Springer Praxis Books. Springer, Berlin, Heidelberg. https://doi.org/10.1007/3-540-27129-5_7, 2005.

[16] Heimsath, A.M., Deitrich, W.E., Nishizumi, K., Frinkel, R.C.: The soil production function and landscape equilibrium, Nature, 388, 358-361, 1997. https://doi.org/10.1038/41056.

[17] Iverson, R. M., LaHusen, R. G.: Dynamic pore-pressure fluctuations in rapidly shearing granular materials, Science, 246, 796-799, https://doi.org/10.1126/science.246.4931.796, 1989.

[18] Iverson, R. M., Reid, M. E., LaHusen, R. G.: Debris-flow mobilization from landslides, Annu. Rev. Earth Planet. Sci., 25, 85-138, https://doi.org/10.1146/annurev.earth.25.1.85, 1997.

[19] Iverson, R.M., Reid. M.E., Logan, M., Lahusen, R.G., Godt, J.W., Griswold, J.P.: Positive feedback and momentum growth during debris-flow entrainment of wet bed sediment, Nature. Geosci., 4(2), 116–121, https://doi.org/10.1038/ngeo1040, 2011.

[20] Larsen, I. J., Montgomery, D. R., Korup, O.: Landslide erosion controlled by hillslope material, Nat. Geosci., 3, 247-251, https://doi.org/10.1038/ngeo776, 2010.

[21] Lee, E., Kim, S. Seasonal and spatial characterization of soil moisture and soil water tension in a steep hillslope, J. Hydrol., 568, 676-685, https://doi.org/10.1016/j.jhydrol.2018.11.027, 2019.

[22] Li, M. Y., Ma, C., Du, C., Yang, W. T., Lyu, L. Q., Wang, X. H.: Landslide response to vegetation by example of July 25-26, 2013, extreme rainstorm, Tianshui, Gansu Province, China, Bull. Eng. Geol. Environ., 80, 751-764, https://doi.org/10.1016/10.1007/s10064-020-02000-9, 2021.

[23] Lu, N., and Godt. J. W.: Hillslope hydrology and stability, Cambridge Univ. Press, Cambridge, UK, 2013.

[24] Lu, N., and Likos, W. J.: Suction stress characteristic of unsaturated soils, J. Geotech. Geoenviron. Eng., 132, 131-142, http://doi.org/10.1061/(ASCE)1090-0241(2006)132:2(131), 2006.

[25] McGuire, L. A., Rengers, F. K., Kean, J. W., Coe, J. A., Mirus, B. B., Baum, R. L., Godt, J. W.: Elucidating the role of vegetation in the initiation of rainfall-induced shallow landslides: insights from an extreme rainfall event in the Colorado front range, Geophys. Res. Lett., 43, 9084-9092, https://doi.org/10.1002/2016GL070741, 2016.

[26] Milledge, D. G., Bellugi, D., McKean, J. A., Densmore, A. L., Dietrich, W. E.: A multidimensional stability model for predicting shallow landslide size and shape across landscapes, J. Geophys. Res.: Earth Surf., 119, 2481-2504, https://doi.org/10.1002/2014JF003135, 2014.

[27] Montgomery, D. R., Dietrich, W. E.: Landscape dissection and drainage area-slope thresholds, In: Kirkby MJ (ed) Process models and theoretical geomorphology, John Wiley, Hoboken, N. J., pp: 221-246, 1994.

[28] Mualem, Y.: Hysteretical models for prediction of the hydraulic conductivity of unsaturated porous media, Water Resour. Res., 12, 1248-1254, https://doi.org/10.1029/WR012i006p01248, 1976.

[29] Rengers, F. K., McGuire, L. A., Coe, J. A., Kean, J. W., Baum, R. L., Staley, D. M., Godt, J. W.: The influence of vegetation on debris-flow initiation during extreme rainfall in the northern Colorado front range, Geology, 44, 823-826, http://doi.org/10.1130/G38096.1, 2016.

[30] Sassa, K.: The mechanism starting liquefied landslides and debris flows. Proceedings of 4th International Symposium on Landslides, Toronto, Canada, vol. 2, pp. 349-354, 1984.

[31] Schmidt, K. M., Roering, J. J., Stock, J. D., Dietrich, W. E., Montgomery, D. R., Schaub, T.: The variability of root cohesion as an influence on shallow landslide susceptibility in the Oregon Coast Range, Can. Geotech., 38, 995-1024, http://doi.org/10.1139/cgi-38-5-995, 2001.

[32] Schwinning, S.: The ecohydrology of roots in rocks, Ecohydrology: Ecosystems, land and water process interactions, Ecohydrology, 3, 238-245,https://doi.org/10.1002/eco.134,2010.

579    [33] Terzaghi, K.: Mechanism of landslides. In: Paige, S. (Ed.), Application of Geology to Engineering Practice
580        (Berkey Volume). Geological Society of America, New York, pp. 83-123, 1950.

581    [34] Timilsina, S., Niemann, J. D., Rathburn, S. L., Rengers, F. K., Nelson, P. A.: Modeling hydrologic processes
582        associated with soil saturation and debris flow initiation during the September 2013 storm, Colorado Front
583        Range, Landslides, 18, 1741-1759, https://doi.org/10.1007/s10346-020-01582-5, 2021.

584    [35] Van Genuchten, M. T.: A closed-form equation for predicting the hydraulic conductivity of unsaturated soils,
585        Soil Sci. Soc. Am. J, 44, 892-898, https://doi.org/10.2136/sssaj1980.03615995004400050002x, 1980.

586    [36] Wang, C. Y.: Study on the relationship between aspect and slope stability, Dissertation, Kunming University
587        of Science and Technology, 2008 (in Chinese).

588    [37] Wang, G. H., Sassa, K.: Pore-pressure generation and movement of rainfall-induced landslides: effects of grain
589        size and fine-particle content, Eng. Geol., 69, 109-125, https://doi.org/10.1016/S0013-7952(02)00268-5, 2003.

590    [38] Wang, X. H., Ma, C., Wang, Y. Q., Wang, Y. J., Li, T., Dai, Z. S., Li, M. Y.: Effect of root architecture on
591        rainfall threshold for slope stability: variabilities in saturated hydraulic conductivity and strength of root-soil
592        composite, Landslides, 17, 1965-1977, https://doi.org/10.1007/s10346-020-01422-6, 2020.

593    [39] Watakabe, T., Matsushi, Y.: Lithological controls on hydrological processes that trigger shallow landslides:
594        Observations from granite and hornfels hillslopes in Hiroshima, Japan, Catena, 180: 55-68,
595        https://doi.org/10.1016/j.catena.2019.04.010, 2019

596    [40] Wayllace, A., Lu, N.: A transient water release and imbibtions method for rapidly measuring wetting and
597        drying soil water retention and hydraulic conductivity functions. Geotech. Test. J., 35, 1-15, 2012.

598    [41] Yu, G. Q., Zhang, M. S., Hu, W.: Analysis on the development characteristics and hydrodynamic conditions
599        for massive debris flow in Tianshui, Northwest Geol., 47, 185-191, 2014 (in Chinese)